Vortex shedding in flow past an inclined flat plate at high incidencea)

Dan Yang, Bjørnar Pettersen, Helge I. Andersson, and Vagesh D. Narasimhamurthy

Citation: Physics of Fluids (1994-present) **24**, 084103 (2012); doi: 10.1063/1.4744982
View online: http://dx.doi.org/10.1063/1.4744982
View Table of Contents: http://scitation.aip.org/content/aip/journal/pof2/24/8?ver=pdfcov
Published by the AIP Publishing

Vortex shedding in flow past an inclined flat plate at high incidence[a)]

Dan Yang,[1,b)] Bjørnar Pettersen,[1] Helge I. Andersson,[2] and Vagesh D. Narasimhamurthy[2]
[1]*Department of Marine Technology, Norwegian University of Science and Technology, Trondheim NO-7491, Norway*
[2]*Department of Energy and Process Engineering, Norwegian University of Science and Technology, Trondheim NO-7491, Norway*

(Received 14 December 2011; accepted 5 July 2012; published online 21 August 2012)

The properties of asymmetric wake patterns behind a flat plate inclined at angles of attack 20°, 25°, and 30° are investigated. The Reynolds number based on the inflow velocity and the plate width is 1000. Both two-dimensional and three-dimensional calculations are performed by direct numerical simulations. Compared to the three-dimensional simulations, the two-dimensional calculations predict a significantly lower pressure on the rear surface of the plate, which consequently leads to very high drag and lift forces on the plate. The asymmetric mean wake flow, turbulence properties, and coherent patterns in the three-dimensional simulations are analysed by time- and phase-averaged techniques. Unlike the symmetric wake flow, the vortices shed from the leading and trailing edges of an inclined plate possess unequal strength with the trailing edge vortex having higher strength. It is observed that the present three-dimensional simulations predict results which compare well with the experimental data. In addition, wake instabilities in the form of oblique modes and vortex dislocations are observed in the 20° angle of attack case. It is found that this intrinsic instability is most likely due to the low incidence angle rather than the prevailing low Reynolds numbers. © *2012 American Institute of Physics*. [http://dx.doi.org/10.1063/1.4744982]

I. INTRODUCTION

The flow around bluff bodies has received a great deal of attention for over a century due to its practical importance in engineering and scientific relevance in fluid mechanics. From the engineering point of view, there are a number of applications in mechanical, civil, and marine engineering, such as the flow in heat exchangers, around bridge piers and offshore platforms. From the fluid mechanics perspective, the flow around bluff bodies involves various important physical phenomena, such as flow separation, vortex formation, transition to turbulence, and vortex induced vibrations.

It is well established that the flow in the wake of a two-dimensional cylinder exhibits very complicated three-dimensional characteristics even at moderate and high Reynolds numbers. The circular cylindrical structures are the most investigated bluff-body configuration owing to their simple geometry and yet complicated flow features. A large number of both experimental and numerical studies of flow past a circular cylinder have been carried out (see review by Williamson[1]). The flow around other cross-sectional shapes, such as square cylinders, flat plates, and airfoils, also provide considerable interesting flow mechanisms. Najjar and Balachandar[2] performed a three-dimensional

[a)]This manuscript is a substantially expanded and revised version of an unpublished paper with the same title presented by the first author at the 7th International Symposium on Turbulence and Shear Flow Phenomena (TSFP-7) held in Ottawa, Canada in July 2011.
[b)]dan.yang@ntnu.no.

numerical study of the wake behind a normal flat plate at Reynolds number of 250. They observed low frequency unsteadiness in the wake which affected the flow field as well as the global integral parameters such as the Strouhal number and drag coefficient.

A square cylinder or a flat plate inclined relative to the incident free-stream form an asymmetric wake. Tong *et al.*[3] carried out an experimental study of a square cylinder wake and considered the impact of incidence angle variation on wake stability. In the study of Sheard *et al.*,[4] a linear stability analysis is conducted to investigate the wakes behind inclined square cylinders through the three-dimensional transition regime. The early experiments of Fage and Johansen,[5] dealing with a plate at 18 different angles of incidence, showed that the Strouhal number has an approximately constant value of 0.148 at an angle of attack α from 30° to 90°. Vortex shedding occurs from the two edges of an inclined plate, leading to an asymmetric mean velocity field in the very near wake which comprises the recirculation region. It was found that the wake is dominated by a train of counterclockwise vortices shed from the trailing edge of the plate at angle of attack of 30° in the experiments of Lam.[6]

The results from the experimental investigation with a flat plate by Perry and Steiner[7] for an angle of attack of 45°, revealed that the vortex rolling up from the leading edge remained attached to the rear of the plate for a longer period of time than the trailing edge vortex. The experimental investigation of Lam and Leung[8] gave detailed velocity fields obtained with particle-image velocimetry (PIV) at successive phases of a vortex shedding cycle at three angles of attack, 20°, 25°, and 30°, at Reynolds number around 5300. It appeared that the leading edge vortex detached completely from the plate and started its convection in the wake at a location near the trailing edge.

Breuer and Jovicic[9] and Breuer *et al.*[10] simulated the flow over an inclined plate at $\alpha = 18°$, for Reynolds number of 20 000, and their large-eddy simulation (LES) results showed clearly that the wake was strongly dominated by the trailing edge vortices. They also reported that there was no regular shedding of vortices directly at the leading edge. Instead, a Kelvin-Helmholtz instability was detected in the free shear layer behind the leading edge. These shear layer vortices developed into a large recirculation region attached to the leeward side of the plate.

Zhang *et al.*[11] studied the transition route from a steady to a chaotic state of two-dimensional flow past an inclined flat plate at angle of attack in the range of 0°–45°, at Reynolds numbers less than 800. The results revealed a transition process via the sequential occurrence of period-doubling bifurcations and the various incommensurate bifurcations.

From the above it is clear that the asymmetric wake has different flow characteristics and vortex interactions than the symmetric wake pattern. The two trains of vortices separated alternatingly from the leading and trailing edge with opposite sign, have unequal vortex strength. Based on the experiment of Lam and Leung,[8] the different formation mechanisms of the two trains of vortices are believed to result in the different strengths observed. They suggested that the leading edge vortex had undergone a longer birth history and was more diffused, with a lower peak vorticity level at its centre and larger spatial extent of fluid circulation than the trailing edge vortex.

As mentioned previously, in the experiments of Fage and Johansen,[5] it was found that from $\alpha = 30°$ to $\alpha = 90°$, the Strouhal number based on the projected plate width has an approximately constant value 0.148. Furthermore, based on Zhang *et al.*,[11] at angle of attack range of 0°–45°, in the transition from steady to chaotic state, a sequence of successive period doubling bifurcations was detected. In the higher Reynolds number range, the angle of attack range where this complicated process took place was 20°–30°. From the study of Zhang *et al.*,[11] at $\alpha = 25°$, as the Reynolds number increased beyond 730 (which equals to 308.5 based on the projected width), positive Lyapunov exponents were obtained which verify the chaotic flow character.

In the present direct numerical simulation (DNS) study, three angles of attack, i.e., $\alpha = 20°$, 25°, and 30° (consistent with the experiments of Lam and Leung[8]), are adopted while the Reynolds number is 1000 based on the plate width. If we instead adopt the projected width of the plate normal to the incident free-stream as length scale, the Reynolds numbers for the three different angles of attack are 342, 423, and 500. At these Reynolds numbers, the flow could experience different flow regimes. Unlike the partially resolved (LES/DES) data of Breuer and Jovicic[9] and Breuer *et al.*[10] and the partially measured flow-field of Perry and Steiner,[7] Lam,[6] and Lam and Leung,[8] the present study is aimed at fully resolved DNSs and thereby gaining complete access to time-dependent

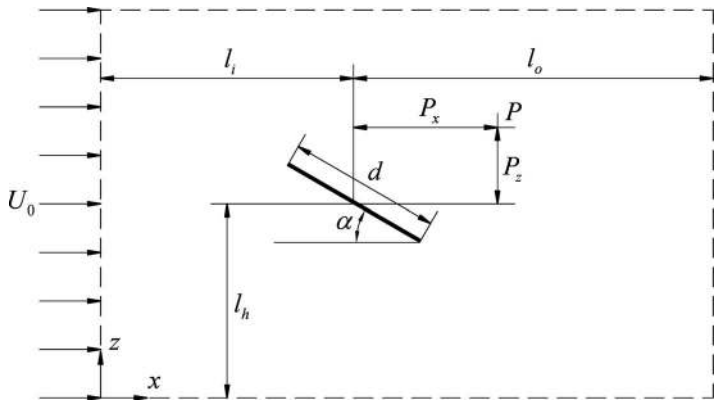

FIG. 1. A schematic representation of the inclined-plate system investigated showing relevant dimensions, freestream flow direction and coordinate system.

three-dimensional data. In addition, previous studies were performed at high Reynolds numbers while we are aiming at relatively low Re flows. Besides the time- and phase-averaged statistics, spectral analysis and three-dimensional vortical structure information will be analysed and presented. Wake instabilities (if any) will also be explored and documented and wherever applicable, the present DNS data will be compared against available experiments.

II. NUMERICAL DETAILS

The problem we consider in the present study is flow around an inclined flat plate, as shown in Fig. 1. The unsteady, incompressible Navier-Stokes equations are non-dimensionalized and solved directly. The non-dimensional variables are defined by the free-stream velocity U_0 and the plate width d and expressed as $u_i = \frac{u_i^*}{U_0}$, $p = \frac{p^*}{\rho U_0^2}$, $x_i = \frac{x_i^*}{d}$, and $t = \frac{t^*}{d/U_0}$. The superscript (*) denotes dimensional quantities. The non-dimensional form of the continuity and Navier-Stokes equations are expressed as

$$\frac{\partial u_i}{\partial x_i} = 0, \tag{1}$$

$$\frac{\partial u_i}{\partial t} + u_j \frac{\partial u_i}{\partial x_j} = -\frac{\partial p}{\partial x_i} + \frac{1}{\mathrm{Re}} \frac{\partial^2 u_i}{\partial x_j \partial x_j}, \tag{2}$$

where the indices $i, j = 1, 2, 3$ refer to the streamwise (x), spanwise (y), and transverse (z) directions of the Cartesian coordinate system, respectively. u is velocity, p is pressure, and t is time. Both two-dimensional and three-dimensional calculations are carried out. The Reynolds number and Strouhal number are defined as $\mathrm{Re} = U_0 d/\nu$, $\mathrm{Re}' = U_0 d \cdot \sin\alpha/\nu$, $St = fd/U_0$, $St' = fd \cdot \sin\alpha/U_0$, where ν is the kinematic viscosity of the fluid, $d' = d \cdot \sin\alpha$ is the projected plate width, and f is the shedding frequency. The thickness of the plate equals to $0.02d$, with sharp (i.e., 90°) leading and trailing edges.

A finite-volume code (Manhart[12]) with non-equidistant Cartesian grids, on which the variables are arranged staggered, is used. The spatial discretization of the convective and diffusive fluxes is based on second-order central differences. The momentum equations are advanced in time by fractional time stepping using a third-order Runge-Kutta scheme. For the representation of the flat plate, an immersed boundary technique is used (Peller *et al.*[13]). The plate geometry is represented by a triangular mesh and the interface cells are searched in a pre-processing algorithm. The immersed boundary technique provides a smooth representation of the body surface by using third-order least squares interpolation for the interface cells.

TABLE I. Domain size parameters and grid resolution compared with previous direct numerical simulations.

	Re	l_i	l_o	$2l_h$	L_y	N_x	N_y	N_z
Najjar and Vanka[14]	1000	8	20	16	2π	256	32	256
Najjar and Balachandar[2]	250	5	20	16	2π	192	48	128
Narasimhamurthy and Andersson[15]	750	5	20	16	6	512	60	384
Present study	1000	5	20	15	6	672	80	474

The computational domain is $25d \times 6d \times 15d$ in x, y, and z direction. The upstream, downstream and transverse domain sizes (l_i, l_o, $2l_h$) are $5d$, $20d$, and $15d$ as shown in Fig. 1. The domain size is based on previous simulations listed in Table I.

In the study of Yang *et al.*,[16] the flow over a flat plate inclined at an angle of attack $\alpha = 25^\circ$ was simulated. A spanwise domain size $L_y = 6d$ was adopted with the number of grid cells equal to 72. This study identified the wave-length of the dominant vortical structure in the spanwise direction to be $0.708d$ at $\mathrm{Re} = 350$ and $0.896d$ at $\mathrm{Re} = 800$, respectively. These results are comparable to the study of Hoarau *et al.*[17] for a NACA0012 aerofoil at $\mathrm{Re} = 800$ and $\alpha = 20^\circ$ where the spanwise wavelength was $0.64d$, and Kitsios[18] for a NACA0015 aerofoil at $\mathrm{Re} = 800$ and $\alpha = 18^\circ$ with a spanwise wavelength of $0.66d$. In both of these studies, the spanwise domain sizes were $4d$. Given these points, it is expected that the spanwise domain size and resolution are sufficient to capture the key spanwise wake structures.

Results from the grid convergence study are listed in Table II. The parameters show only a minor change between the two finest grids. In the present study we use the number of grid points (N_x, N_y, N_z) $672 \times 80 \times 474$ with the smallest grid size being $0.005d$ around the plate surface. The computed time step is $0.001d/U_0$. The location P where the sampled signals are taken is shown in Fig. 1, with $P_x = 1.5d$ and $P_z = 0.5d$ measured from the centre of the plate.

At the inlet, a uniform free-stream velocity profile ($u = U_0$, $v = w = 0$) is assumed. At the outlet boundary, a Neumann boundary condition ($\partial u_i/\partial x = 0$) is used for all the velocity components and the pressure is set to zero. No-slip conditions are prescribed at the body surface. At top and bottom boundaries, we adopt the slip conditions ($\partial u/\partial z = \partial v/\partial z = \partial p/\partial z = 0$, $w = 0$). In the spanwise direction, a periodic boundary condition is imposed. For the two-dimensional calculations the domain size is also $25d$ in the streamwise direction and $20d$ in the transverse direction to capture the vortex pairing dynamics in the wake.

III. RESULTS AND DISCUSSION

In this section, results from simulations at three different angles of attack at a Reynolds number $\mathrm{Re} = 1000$ will be presented. In order to first address the vortex dynamics, instantaneous results are presented in Sec. III A, whereas time-averaged and phase-averaged results are reported in Secs. III B and III C, respectively. The majority of the results are from three-dimensional Navier-Stokes solutions, i.e., DNS. Comparisons are occasionally made with solutions of the two-dimensional Navier-Stokes equations.

TABLE II. Study on influence of grid resolution on integral parameters, at $\alpha = 25^\circ$ and $\mathrm{Re} = 1000$.

	$(\Delta x_{\min}, \Delta z_{\min})$	Δy	$\bar{C}_D$	$\bar{C}_L$	St
$448 \times 48 \times 367$	0.008	0.125	0.4540	1.0765	0.4044
$576 \times 48 \times 450$	0.005	0.125	0.4603	1.1189	0.4120
$576 \times 72 \times 450$	0.005	0.083	0.4598	1.1173	0.4158
$672 \times 80 \times 474$	0.005	0.075	0.4595	1.1163	0.4196

A. Instantaneous results

In Figs. 2(a), 2(c), and 2(e) the temporal variations of the streamwise velocity component are plotted for three different angles of attack, measured at the downstream point $x = 6.5d$, $y = 2d$, $z = 8d$, which is located behind the plate on the leading edge (upper) side. The corresponding autocorrelations of the streamwise velocity component signals are defined by $A(T) = \frac{\overline{u(t)u(t+T)}}{\overline{u(t)^2}}$ and are shown in Figs. 2(b), 2(d), and 2(f). Oscillations in the streamwise velocity component for the three different angles of attack show a distinct shedding frequency of the flow. The periodicity in the autocorrelation shows that the flow reaches a relative stable state with almost constant oscillation amplitude at $\alpha = 25^\circ$ and 30°, Figs. 2(d) and 2(f). However, for $\alpha = 20^\circ$ in Fig. 2(b), low frequency modulations can be observed at intermittent random time-intervals indicating wake instabilities.

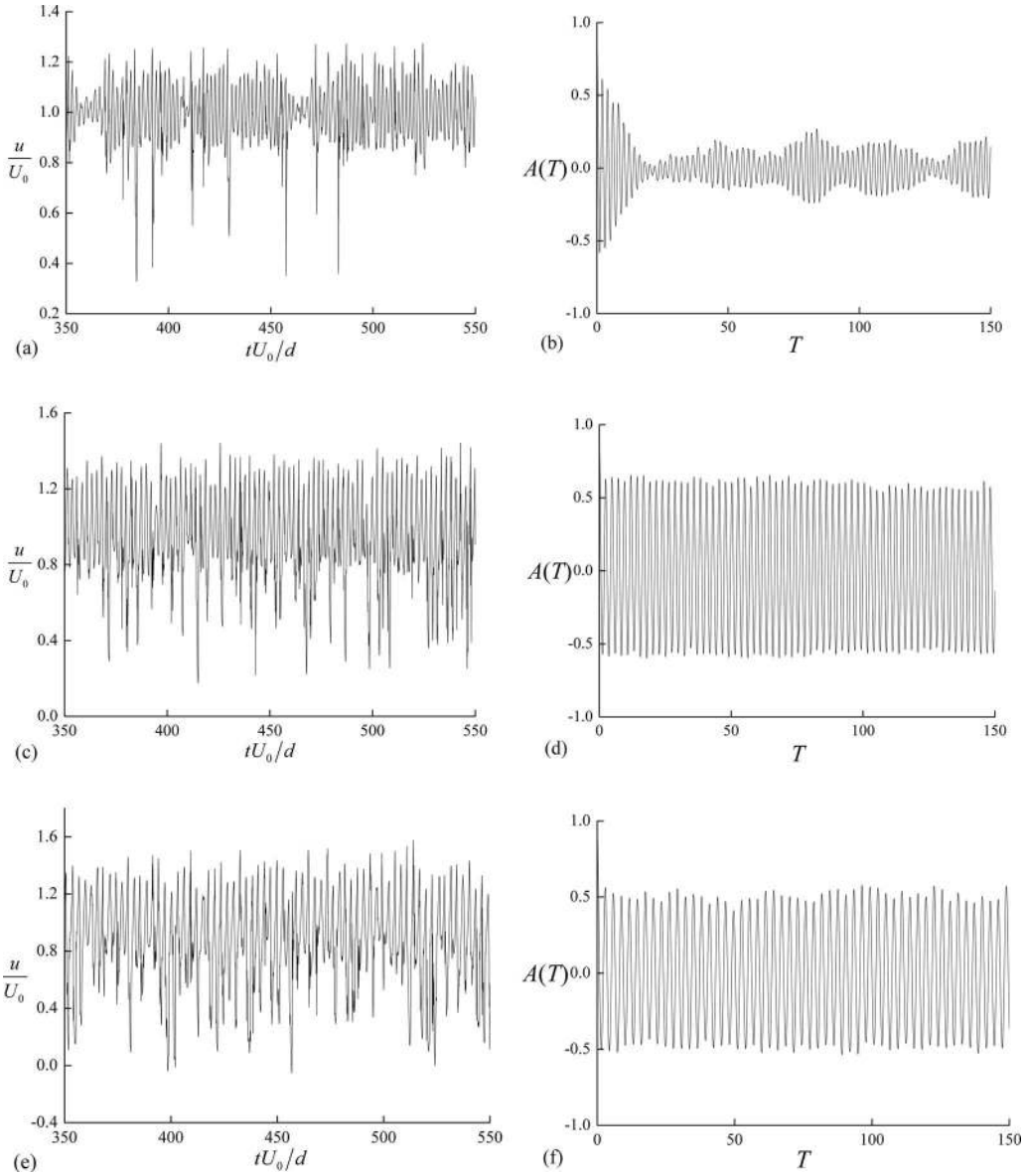

FIG. 2. Time signals of the streamwise velocity component at three angles of attack, (a) $\alpha = 20^\circ$, (c) $\alpha = 25^\circ$, and (e) $\alpha = 30^\circ$. Corresponding autocorrelations $A(T)$ of the velocity signals are shown in (b), (d), and (f).

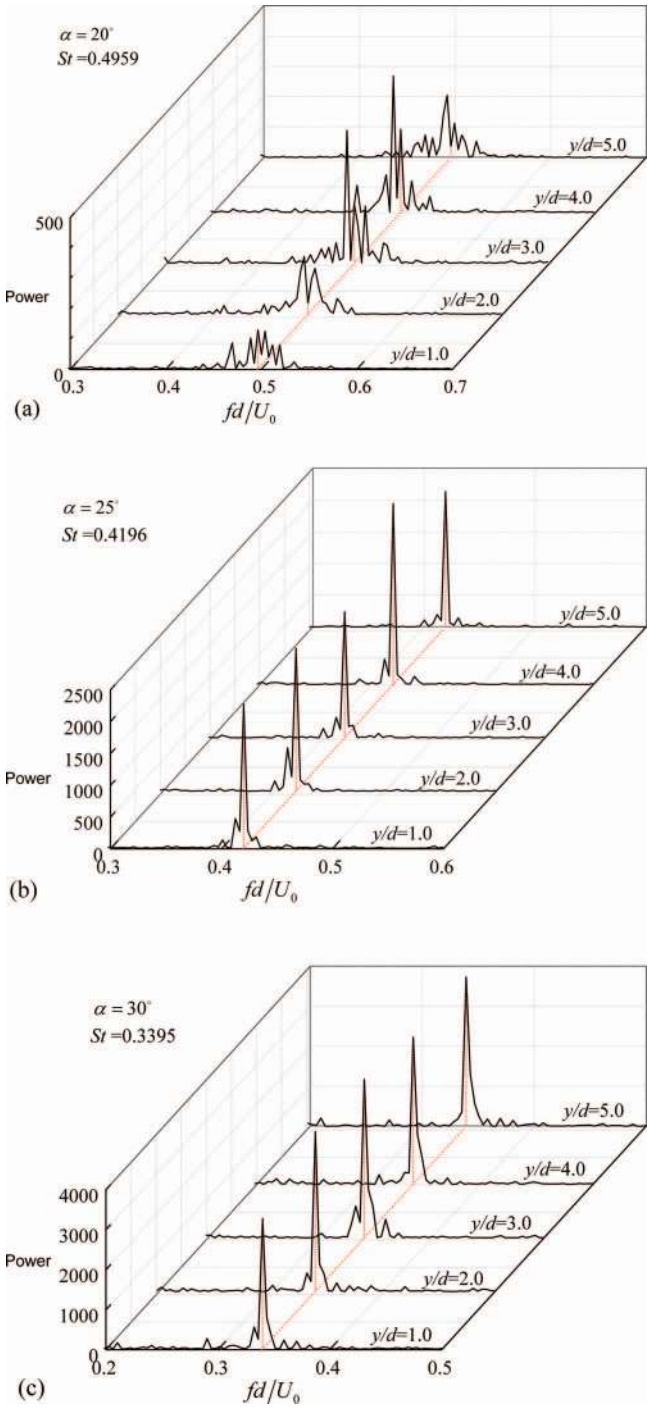

FIG. 3. Frequency spectra of the transverse velocity component w at different spanwise (y/d) positions, (a) $\alpha = 20^\circ$, (b) $\alpha = 25^\circ$, and (c) $\alpha = 30^\circ$. The dotted lines indicate the spanwise-averaged frequency at the three angles of attack ($St = 0.4959$, 0.4196, and 0.3395, respectively).

Figure 3 shows the frequency spectra of the transverse velocity component along the span for the three angles of attack. The streamwise and transverse positions at which the velocity signals are taken are the same as in Fig. 2. The time period used to perform the fast Fourier transform was approximately equal to 130 times the vortex shedding cycle. For angle of attack $\alpha = 20^\circ$, a significant broadening of the spectrum with multiple peaks in some positions (at $y/d = 3.0 - 4.0$ in Fig. 3(a)) can be identified, and strong variations in the peak value can be observed along the

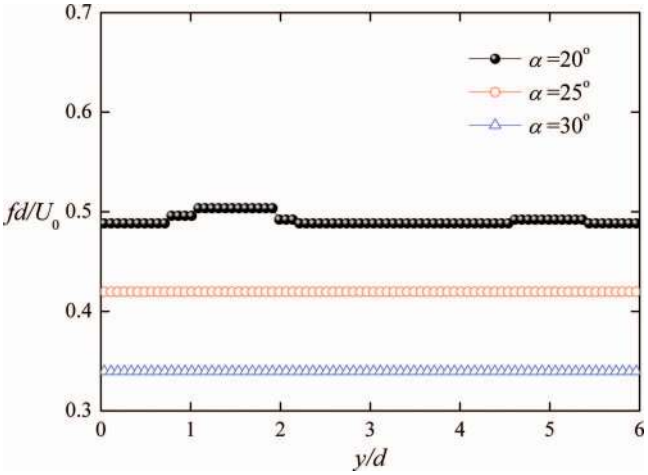

FIG. 4. Predominant vortex shedding frequency across the span for the three angles of attack.

span. For angle of attack $\alpha = 25^\circ$ and 30°, a single spectral peak can be identified and only modest variations in the peak value can be observed along the span.

In the present simulation, the vortex shedding in the flow around the plate at angle of attack $\alpha = 20^\circ$ does not maintain a constant shedding frequency in the spanwise direction (see Fig. 3(a)). Figure 4 shows the predominant vortex shedding frequency across the span for all three angles of attack. A slight frequency difference along the span can be seen for $\alpha = 20^\circ$ which relates to discontinuities and oblique shedding in the wake. This phenomenon could be seen clearly from Figs. 5(a) and 5(b). Such vortex dislocations and oblique shedding are known to occur behind two-dimensional bluff bodies either during wake transition (Williamson[19]) or due to non-uniform boundary conditions (Huang *et al.*[20]), and also behind three-dimensional bluff bodies (Narasimhamurthy *et al.*[21,22]).

To address the three-dimensional vortical structures, the instantaneous iso-surfaces of $-\lambda_2$ are shown in Fig. 5 for different angles of attack. This method for identifying vortex structures is

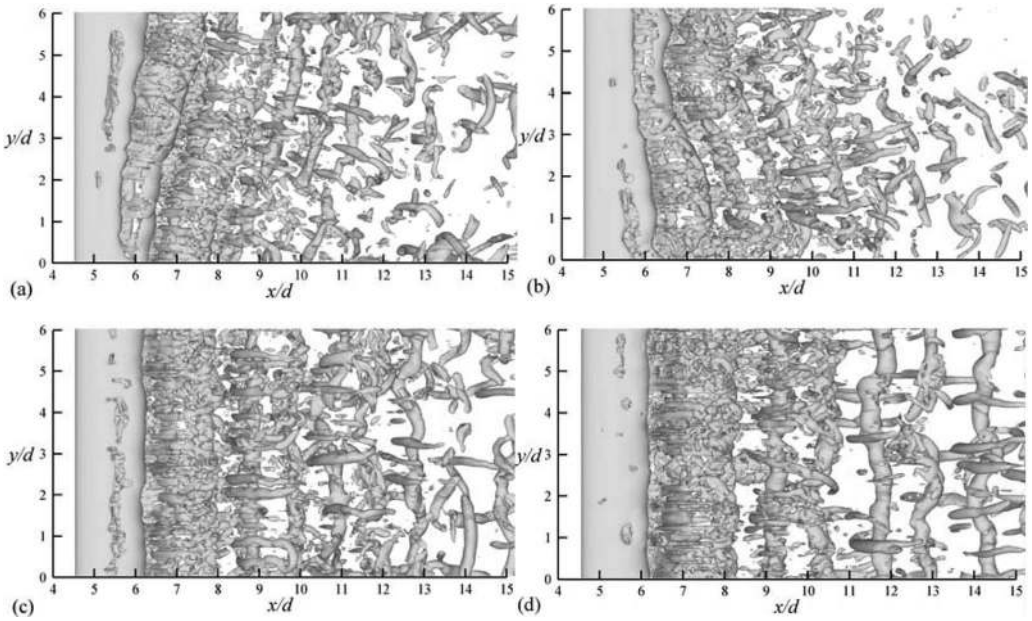

FIG. 5. Top view of the instantaneous iso-surface of $-\lambda_2$, at (a) angle of attack $\alpha = 20^\circ$, $t = 400$, (b) $\alpha = 20^\circ$, $t = 700$, (c) $\alpha = 25^\circ$, $t = 600$, and (d) $\alpha = 30^\circ$, $t = 600$.

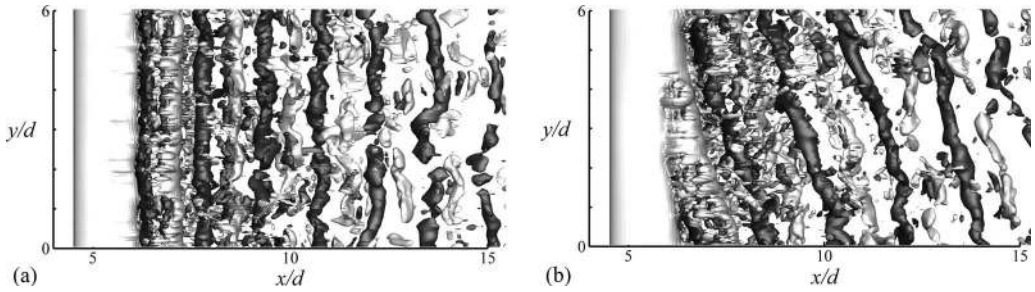

FIG. 6. Iso-surface of the spanwise vorticity component at (a) $\alpha = 18^\circ$ and (b) $\alpha = 22^\circ$. Re $= 1000$ in both cases.

described in Jeong and Hussain.[23] In Figs. 5(a) and 5(b) for $\alpha = 20^\circ$, it can be observed that the spanwise vortex rollers are shed obliquely at an angle to the plate. The oblique angles are random. On the contrary, for $\alpha = 25^\circ$ and 30° in Figs. 5(c) and 5(d), respectively, the shed vortex rollers are parallel with the plate and continuous along the whole span. In addition to the characteristic von Kármán vortices, braids comprising streamwise vorticity connecting the von Kármán rollers can be observed. For Re $= 1000$, cases for angle of attack $\alpha = 18^\circ$ and $\alpha = 22^\circ$ are simulated to verify the oblique vortex shedding observed at $\alpha = 20^\circ$. The results which are shown in Fig. 6 demonstrate the same oblique shedding at $\alpha = 22^\circ$, while at $\alpha = 18^\circ$, parallel shedding is predominant as in the case with $\alpha = 25^\circ$ and 30°.

The time trace of the transverse velocity component w along the spanwise direction for $\alpha = 20^\circ$ is shown in Fig. 7. The chosen sampling time is 200 non-dimensional time units d/U_0, starting from when the flow reaches a statistically steady state (which could be seen from Fig. 2). The time period covers around 100 vortex shedding cycles. At the same time, a spatial decomposition technique (Mansy *et al.*[24]) is adopted to extract quantitative information about the secondary component from the total velocity signals. In this procedure, the velocity is separated into two components. One consists of the mean flow and the primary instability, while the other corresponds to the three-dimensional structures. Shown in Fig. 7(a) is the continuous velocity signal and in Fig. 7(b) is the corresponding primary component. The time tracing clearly demonstrates the non-parallel shedding of the wake and the random appearances of phase discontinuities. From Fig. 7, it is found that periods of oblique and parallel shedding appear randomly, where vortex dislocations arise intermittently. The time traces of the transverse velocity are corresponding to the frequency spectra in Fig. 3(a), in which multiple peaks indicated the alternating appearance of parallel and oblique shedding in the wake.

The instantaneous iso-surface of the spanwise vorticity shown in Fig. 8 corresponds to the non-dimensional time instant at $t = 160$ in Fig. 7. Due to the vortex shedding phase difference, two vortex dislocations are observed. This can also be seen from the velocity autocorrelation at this angle in Fig. 2(b), in which a beating pattern is visible.

Instantaneous contours of spanwise vorticity are shown in Fig. 9 taken at the mid span. The fundamental difference between the two- and three-dimensional results is the extended width of the wake in the former. In the three-dimensional simulations the vortex shedding occurs alternatingly at the leading edge and trailing edge and thus forms a regular vortex street in the wake. In the two-dimensional simulations, the secondary instabilities lead to the appearance of a complex aperiodic interaction between the vortices shed from the two edges of the plate and an exceptionally wide wake region is formed. For example at angle of attack $\alpha = 20^\circ$ (Fig. 9(a)), a strong aperiodic behavior occurs, while at angle of attack $\alpha = 30^\circ$ (Fig. 9(e)), the wake vortices pair up due to the asymmetry of the body, and then self-propel obliquely to the free-stream. This gives the appearance of a deflected wake. The vortex shedding frequencies are compared with the experimental results of Lam and Leung[8] (at Re ≈ 5300) in Table III. For the present study the Strouhal number is consistently lower in the two-dimensional simulations than in the three-dimensional simulations. The Strouhal number St decreases monotonically with increasing angle of attack, whereas St' is almost independent of α in the 3D cases.

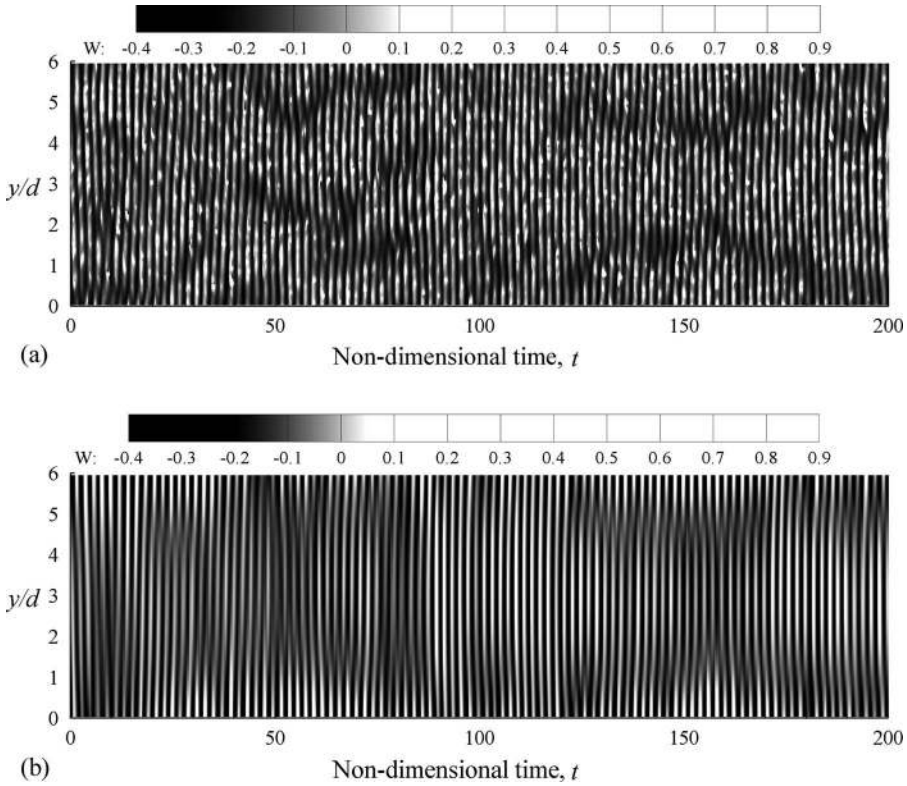

FIG. 7. (a) Time traces of the continuous transverse velocity component w along the spanwise direction at angle of attack $\alpha = 20°$. (b) The primary part of the velocity component extracted from the total shown in (a) by the spatial decomposition technique. The time-origin $t = 0$ corresponds to the dimensionless time value 400.

B. Time-averaged flow fields

In Fig. 10, the mean pressure coefficient, $\bar{C}_p = 2(\bar{p} - p_0)/\rho U_0^2$, based on the time- and span-averaged non-dimensional pressure from the three-dimensional simulations at the three angles of attack is plotted around the plate surface. Also presented are the two-dimensional simulation results, the LES data of Breuer and Jovicic[9] at angle of attack $\alpha = 18°$ and the experimental data of Fage and Johansen[5] at angle of attack $\alpha = 30°$. The current three-dimensional simulations compare well with the simulation data and the experimental data, whereas the two-dimensional simulations predict a significantly lower base pressure and do not capture the almost uniform distribution of the pressure along the rear side of the plate as in the normal plate calculation of Najjar and Balachandar[2] and

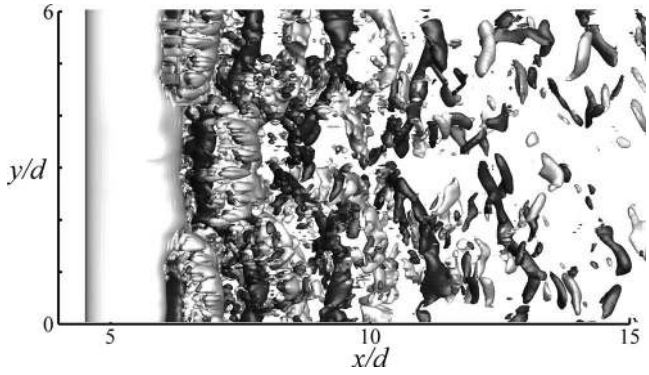

FIG. 8. Iso-surface of spanwise vorticity component at $\alpha = 20°$ and $t = 560$.

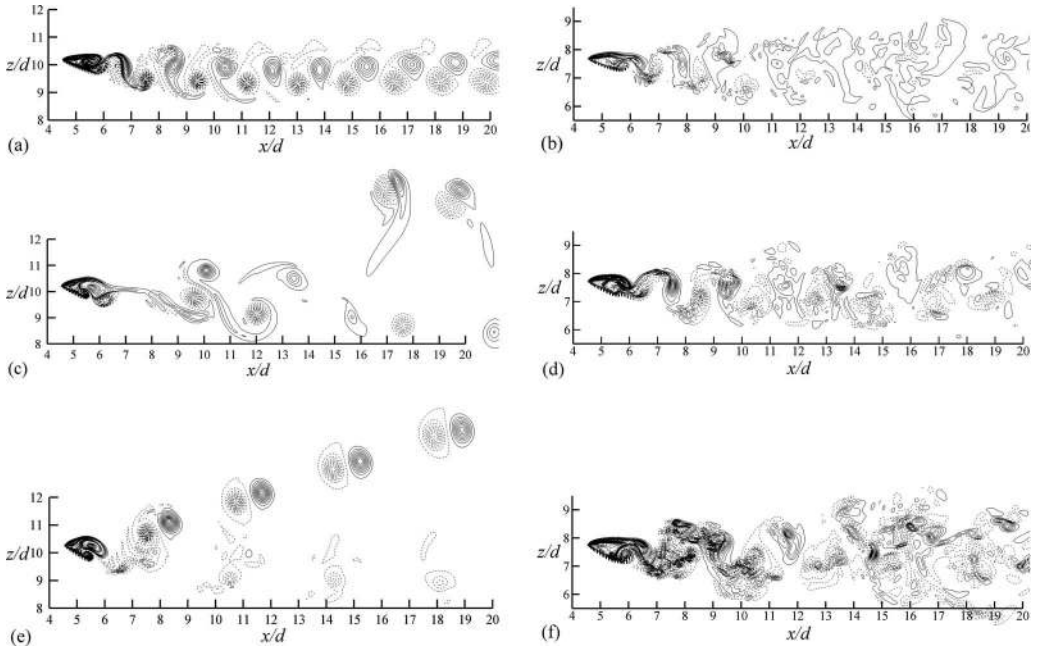

FIG. 9. Contour plots of instantaneous spanwise vorticity in the near wake of the inclined flat plate computed from (a), (c), and (e) two-dimensional simulations and (b), (d), and (f) three-dimensional simulations, at attack angle of (a) and (b) $\alpha = 20^\circ$, (c) and (d) $\alpha = 25^\circ$, (e) and (f) $\alpha = 30^\circ$. The vorticity contours from the three-dimensional simulations are at the mid span. Solid (dashed) contours represent clockwise (counterclockwise) rotation. The horizontal and the vertical axes represent the streamwise and the transverse direction, respectively.

Narasimhamurthy and Andersson.[15] This deficiency becomes worse as the angle of attack increases, especially near the trailing edge.

The almost constant pressure in the base region measured in the experiment is well captured by the three-dimensional simulation. The non-uniform pressure distribution along the base and the higher suction in the two-dimensional simulation make the plate experience higher lift and drag forces, as presented in Table III. At angle of attack $\alpha = 30^\circ$, for instance, the drag force is overpredicted by almost 100%. In the present paper at Re = 1000, the Strouhal number St', based on the projection of the plate width normal to the flow, does not show an angle of attack dependence, which could indicate a different flow regime than at the higher Re $\sim 10^5$ (Lam and Leung[8]). This may explain the differences between the simulations and the experimental results in Table III.

TABLE III. Comparison of integral quantities for two-dimensional and three-dimensional simulations at different angles of attack.

Method	Re	α	Dimension	$\bar{C}_D$	$\bar{C}_L$	St	St'
LES (Breuer and Jovicic[9])	20 000	18	3D	0.38	1.12	0.66	0.204
Experiment (Lam and Leung[8])	$\lesssim$10 000	20	...	...	...	...	0.18
Present DNS	1000	20	2D	0.3188	1.0381	0.4883	0.1670
			3D	0.2880	0.9576	0.4959	0.1696
Experiment (Lam and Leung[8])	$\lesssim$10 000	25	...	...	...	...	0.15
Present DNS	1000	25	2D	0.5827	1.3756	0.3967	0.1677
			3D	0.4595	1.1163	0.4196	0.1773
Experiment (Lam and Leung[8])	5000–25 000	30	...	...	...	...	0.14
Present DNS	1000	30	2D	1.1643	2.1156	0.2556	0.1278
			3D	0.6252	1.1902	0.3395	0.1698

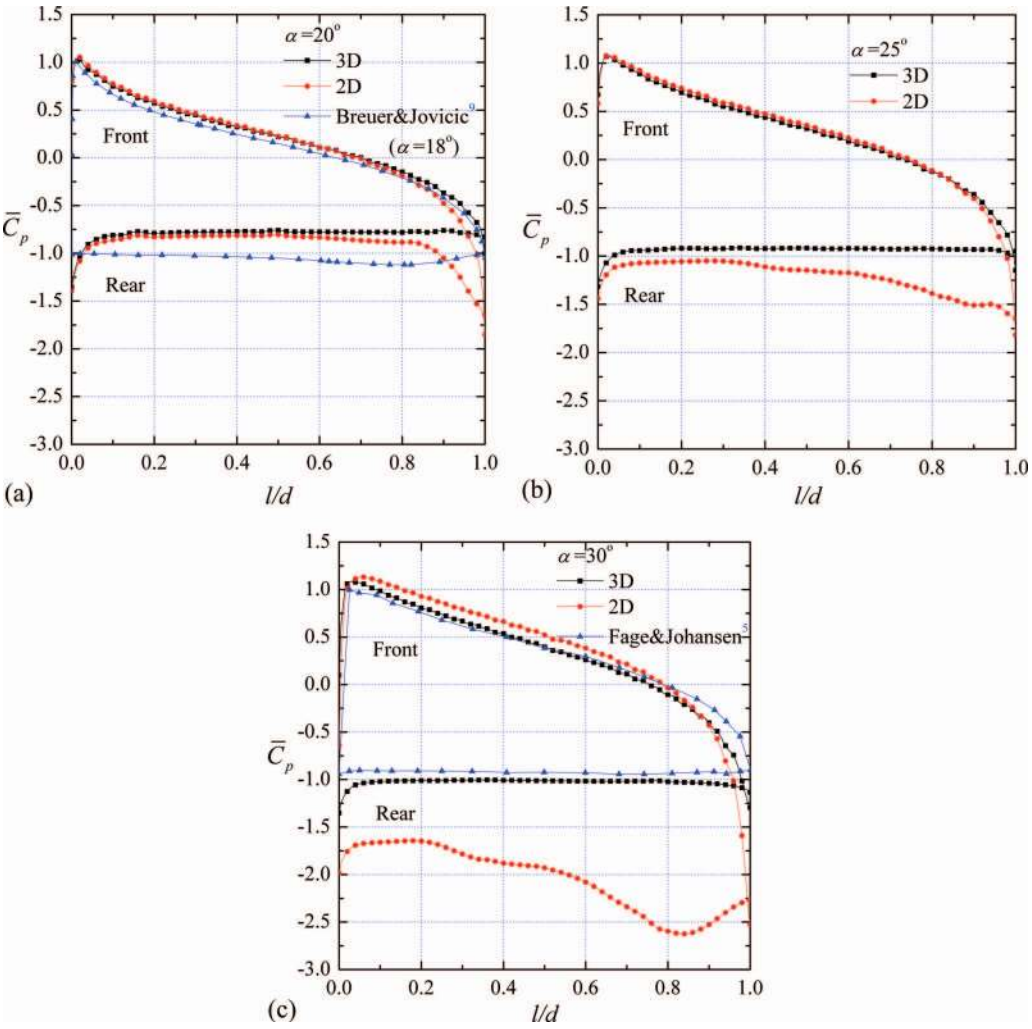

FIG. 10. Distribution of the mean pressure coefficient $\bar{C}_p$ along the plate surface obtained from both two-dimensional (2D) and three-dimensional (3D) simulations and experiments by Breuer and Jovicic[9] and Fage and Johansen.[5]

Figure 11 shows the different components of non-dimensional time- and span-averaged Reynolds stress tensor at the three different angles of attack from the three-dimensional simulations. Also plotted are the separating streamlines of the mean flow so that the Reynolds stresses associated with the mean wake recirculation region can be seen. The peak magnitudes of the shear stress $\overline{u'w'}$ are 0.132, 0.121, and 0.148, in Figs. 11(a), 11(c), and 11(e), at angle of attack $\alpha = 20^\circ$, 25°, and 30°, respectively. These values are of the same order of magnitude as that of the flat plate placed normal to the uniform flow at Re = 250 (Balachandar *et al.*[25]) in which a value of 0.13 was reported for the shear stress. In the present calculation, $\overline{u'w'}$ has the peak value of 0.148 and 0.107 on the leading and trailing edge side, respectively, at angle of attack $\alpha = 30^\circ$. This peak difference is about 4.1% of U_0^2 and higher than at the other two angles, in which the peak differences are 1.6% and 0.8% of U_0^2, respectively. The maximum shear stress is observed on the trailing edge side at angle of attack $\alpha = 20^\circ$ and 25°, whereas it is on the leading edge side at angle of attack $\alpha = 30^\circ$.

The corresponding non-dimensional Reynolds normal stresses are shown in Figs. 11(b), 11(d), and 11(f). The peak values of $\overline{u'u'}$ and $\overline{w'w'}$ at the three different angles of attack are 0.15 and 0.28 at $\alpha = 20^\circ$, 0.19, and 0.42 at $\alpha = 25^\circ$ and 0.24 and 0.47 at $\alpha = 30^\circ$. Apparently these peak values increase as the angle of attack increases, especially for the transverse normal stress. The corresponding peak values for a normal plate at Re = 250 are 0.23 and 0.42 (Balachandar *et al.*[25]). In all the cases, the peak transverse normal stress is higher than the streamwise component and the

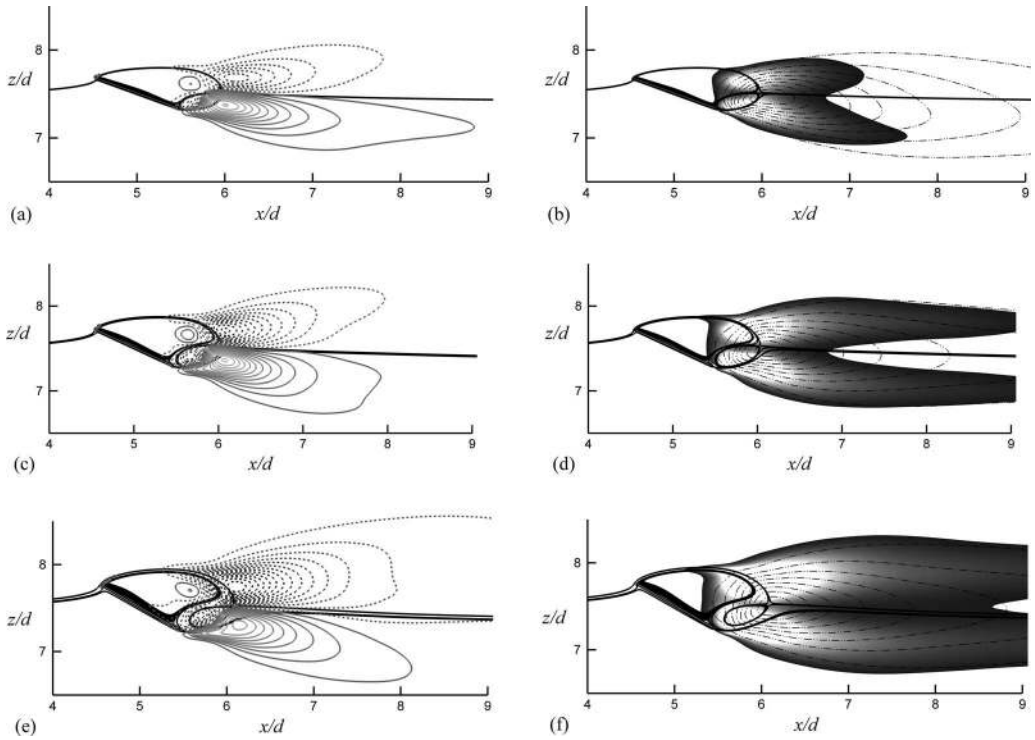

FIG. 11. Reynolds stress distribution, (a) $\overline{u'w'}/U_0^2$, (b) $\overline{u'u'}/U_0^2$ and $\overline{w'w'}/U_0^2$ at $\alpha = 20^\circ$; (c) $\overline{u'w'}/U_0^2$, (d) $\overline{u'u'}/U_0^2$ and $\overline{w'w'}/U_0^2$ at $\alpha = 25^\circ$; (e) $\overline{u'w'}/U_0^2$, (f) $\overline{u'u'}/U_0^2$ and $\overline{w'w'}/U_0^2$ at $\alpha = 30^\circ$. Filled contours correspond to streamwise normal stress and dashed-dotted lines correspond to transverse normal stress in (b), (d), and (f). The outline of the mean recirculation region has been superimposed by the solid lines in all figures. The horizontal and the vertical axes represent the streamwise and the transverse direction, respectively.

difference between them is higher at angle of attack $\alpha = 25^\circ$ and 30°. It is furthermore observed from the Reynolds stress plots that the shear stress is not antisymmetric and the normal stresses are not symmetric about the wake centerline because of the plate inclination.

C. Phase-averaged flow fields

In order to facilitate the interpretation of the results, the phase-averaging technique is adopted to obtain the mean values at constant phases. Based on the triple-decomposition scheme of Reynolds and

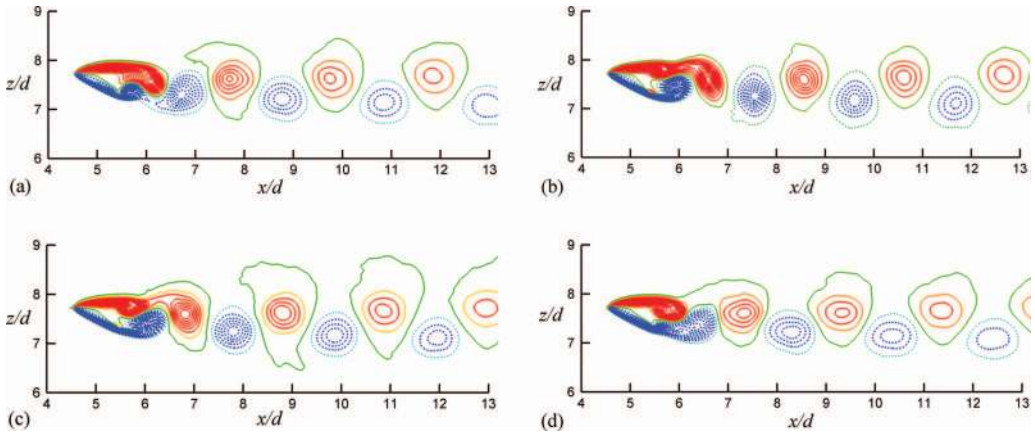

FIG. 12. Phase-averaged spanwise vorticity contour at angle of attack $\alpha = 25^\circ$, figures (a)–(d) show consecutive phases in a single period. The horizontal and the vertical axes represent the streamwise and the transverse directions, respectively.

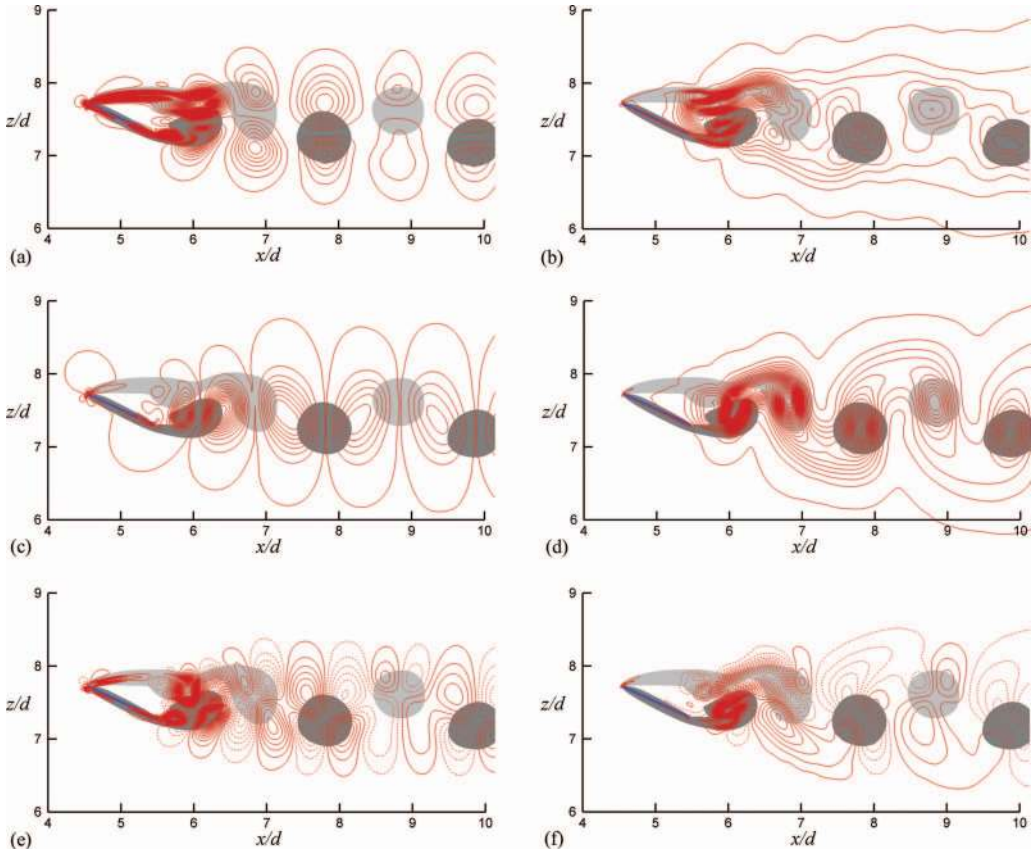

FIG. 13. Phase-averaged contour lines for Reynolds stresses of angle of attack $\alpha = 25^\circ$ at constant phase in Fig. 12(c), dotted contours for negative values. (a) $\tilde{u}\tilde{u}/U_0^2$, (b) $\langle u'u'\rangle/U_0^2$, (c) $\tilde{w}\tilde{w}/U_0^2$, (d) $\langle w'w'\rangle/U_0^2$, (e) $\tilde{u}\tilde{w}/U_0^2$, and (f) $\langle u'w'\rangle/U_0^2$. The vortex cells are shown by background vorticity regions (in light and dark grey). The horizontal and the vertical axes represent the streamwise and the transverse direction, respectively.

Hussain,[26] the flow velocity signals consist of a time-averaged component $\bar{u}$, a coherent component $\tilde{u}$ and an incoherent random (turbulent) component u'. Ensemble averaging at different phases separates the random component and leaves the phase-averaged velocity $\langle u\rangle$, which contains the time-averaged and coherent component, i.e., $\langle u\rangle = \bar{u} + \tilde{u}$. In this process, each vortex shedding cycle is divided into 16 time intervals. The velocity field is the ensemble average of all snapshots at the same phase. The simulations extend 50 vortex shedding cycles to ultimately gain the phase-averaged results.

Contours of phase- and span-averaged spanwise vorticity at four consecutive phases are depicted in Fig. 12. It is shown that two trains of vortices with opposite senses of rotation are evident. The trailing edge vortex is formed by roll-up of the shear layer and shed directly from the roll-up location. The shear layers formed at the leading edge extend along the streamwise direction over some distance and develop into a large recirculation cell. This clockwise vortex remains attached to the plate and only sheds after the interaction with the oppositely rotating trailing edge vortex.

From the momentum equation for the mean flow at constant phase, the Reynolds stresses $\langle u_i' u_j' \rangle$ are important from the point of view of the coherent structures and generated by spatially local random fluctuations at constant phase. Of equal importance from the point of view of conventional turbulence modeling is $\tilde{u}_i\tilde{u}_j$, which is needed along with $\langle u_i' u_j' \rangle$ for any inquiry into the relative contributions of the periodic and random motions to Reynolds-stress terms in the global mean-momentum equation (Cantwell and Coles[27]).

Figures 13(a), 13(c), and 13(e) show the three Reynolds stresses $\tilde{u}\tilde{u}$, $\tilde{w}\tilde{w}$, and $\tilde{u}\tilde{w}$ corresponding to the phase in Fig. 12(c) for the periodic motion. In Fig. 13(a), the vortex phase motion is essentially a local rotation (with respect to the global mean). This rotation generates peaks in the $\tilde{u}\tilde{u}$ contours

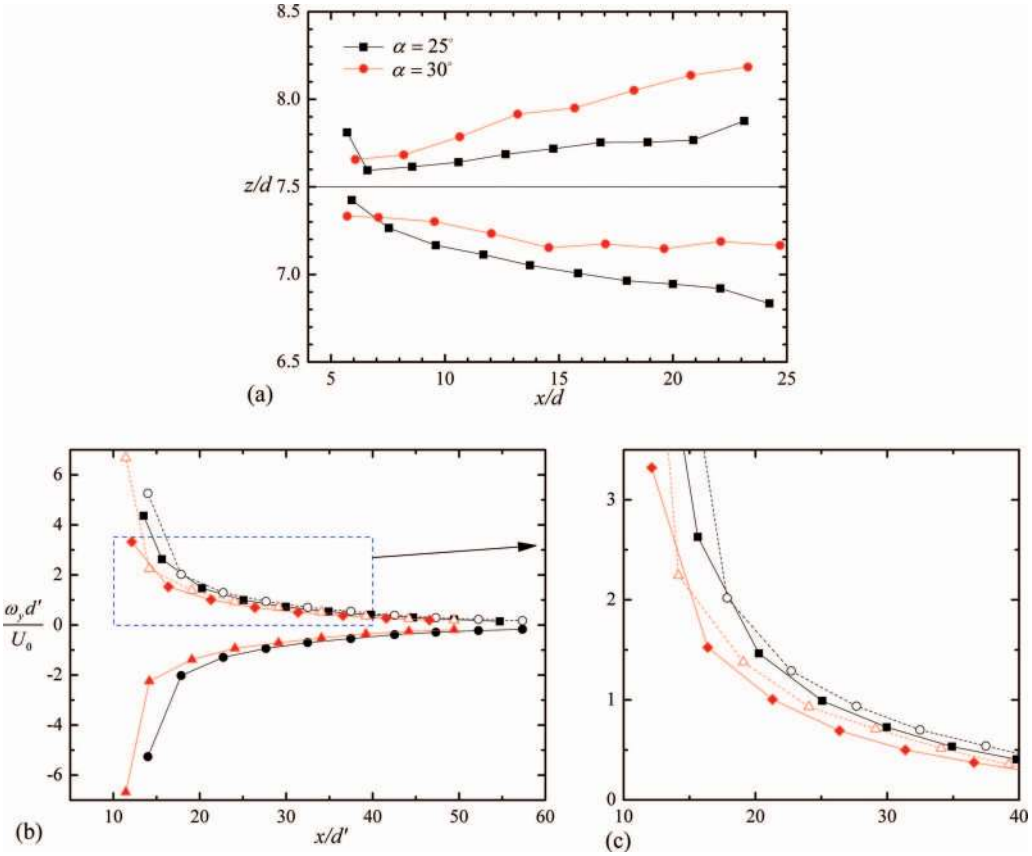

FIG. 14. (a) Phase-averaged spanwise vorticity centre locations. (b) Downstream drop of spanwise peak vorticity levels at vortex centres at $\alpha = 25°$: ■, leading edge vortex; ●, trailing edge vortex; ○, magnitude of trailing edge vortex; $\alpha = 30°$: ♦, leading edge vortex; ▲, trailing edge vortex; △, magnitude of trailing edge vortex. (c) The enlarged view of the amplitudes in (b).

above and below each vortex, with $\tilde{u}$ positive for one peak and negative for the other. The strength of the peaks is evidently unequal. For example the peaks above and below the first counterclockwise vortex are 0.3317 and 0.1130. Similarly, the alternating peaks in $\tilde{w}\tilde{w}$ correspond to the positive and negative peaks in $\tilde{w}$ shown in Fig. 13(c), and the peaks at $x/d = 6.4$, 7.2, 8.3, and 9.4 are 0.4606, 0.2598, 0.1897, and 0.1438, respectively. Figure 13(e) shows the two contributions to the Reynolds shear stress $\tilde{u}\tilde{w}$. Associated with the periodic motion, the stress does not exhibit total antisymmetry, because of the unequal vortex strength. Figures 13(b) and 13(d) show the random streamwise and transverse fluctuations $\langle u'u' \rangle$ and $\langle w'w' \rangle$. The figures show consistently a series of peaks for $\langle u'u' \rangle$ and $\langle w'w' \rangle$ corresponding to the vortex centres with connecting ridges in between them. Figure 13(d) shows $\langle w'w' \rangle$ with larger amplitude and stronger peaks at the vortex locations. The contribution to the shear stress by the random turbulence $\langle u'w' \rangle$ is shown in Fig. 13(f). Unlike the normal stresses, which due to the random turbulence have a maximum near each vortex centre, the shear stress due to the random turbulence has an extreme value near the saddle between the vortices.

Figure 14 shows the vortex centre locations and the spanwise peak vorticity at the vortex centres as they are convected downstream. At the two angles of attack $\alpha = 25°$ and 30°, the vortex trajectory is not symmetric with respect to the centerline through the plate centre. As the angle of attack increases to 30°, the vortex convection route is inclined to the leading edge side of the wake for both the leading and trailing edge vortices. When moving downstream, the vorticity level, normalized by projected width of the plate d' and velocity U_0 as in Lam and Leung,[8] decays with the growth in vortex size by turbulent actions. The magnitudes of the trailing edge vorticity levels are also plotted

in Fig. 14 in order to compare with the leading edge vortex. It is evident that the trailing edge vortex possesses a slightly higher level of peak vorticity.

IV. CONCLUSIONS

Asymmetric vortex shedding occurs naturally behind non-axisymmetric bluff bodies. To explore the vortex shedding phenomenon and other flow instabilities in distinctly asymmetric wake flows, we have considered the flow past an inclined flat plate oriented with an angle of attack α from 20° and up to 30° with respect to the inflow. This incidence is sufficiently high to allow for vortices to be shed not only from the trailing edge of the plate, as at lower incidence, but also from the leading edge of the plate. Furthermore, a massive and asymmetric separation bubble is established in the Reynolds-averaged flow.

Almost all earlier studies of vortex shedding in flows past inclined flat plates have either been for lower angles of attack or at fairly high Reynolds numbers and either experimental studies or large-eddy or detached-eddy simulations. Our aim was therefore to perform fully resolved simulations (DNS) at an intermediate Reynolds number and for high angles of attack.

By integration of the full Navier-Stokes equations in three-dimensional space and in time at a nominal Reynolds number, i.e., based on the plate width d, equal to 1000, complex unsteady flow fields were observed. The quasi-regular von Kármán-type vortex cells co-existed with overwhelming flow three-dimensionalities. In view of the distinctly three-dimensional flow field resulting from the DNSs, it is not surprising to find that the results from fully resolved, but purely 2D Navier-Stokes solutions, become distinctly different. Neither the flow instabilities nor the vortex dynamics are faithfully reproduced in 2D-simulations and the resulting wake becomes far too wide and with too low base pressure. The flow three-dimensionalities which emerge naturally in the DNS provide excess mixing, higher base pressure, and ultimately a lower drag coefficient. Two-dimensional simulations of complex wake phenomena should therefore be abandoned, at least in the present parameter range.

The Strouhal number St', based on the projection of the plate width normal to the inflow, turned out to be about 0.17 and remain almost independent of the angle of attack. This is in contrast with the PIV data of Lam and Leung[8] who observed that St' decreased from 0.18 at $\alpha = 20°$ to 0.14 at $\alpha = 30°$. The fivefold higher Re in their experiments may explain this difference.

Despite the observed constancy of St', the wake behind the plate with 20° inclination turned out to be distinctly different from the two other cases. The shedding frequency for the $\alpha = 20°$ case varied along the span and the primary roll cells were shed obliquely relative to the plate, and vortex dislocations occurred. At the higher angles of attack, parallel shedding of von Kármán cells was observed with the same shedding frequency all along the span. Phase-averaged results revealed that vortices roll up at the trailing edge of the plate from where they are shed, whereas the shear layer which emerges from the leading edge extends about $1d$ downstream before it rolls up and forms a larger vortex cell than those shed directly from the trailing edge. The peak magnitude of the spanwise vorticity of vortices shedding from the trailing edge is slightly higher than for vortices shedding from the leading edge.

ACKNOWLEDGMENTS

This work has received support from the Research Council of Norway (Program for Supercomputing) through a grant of computing time. We thank the anonymous referees for helpful suggestions.

[1] C. H. K. Williamson, "Vortex dynamics in the cylinder wake," Annu. Rev. Fluid Mech. **28**, 477 (1996).
[2] F. M. Najjar and S. Balachandar, "Low-frequency unsteadiness in the wake of a normal flat plate," J. Fluid Mech. **370**, 101 (1998).
[3] X. H. Tong, S. C. Luo, and B. C. Khoo, "Transition phenomena in the wake of an inclined square cylinder," J. Fluids Struct. **24**, 994 (2008).
[4] G. J. Sheard, M. J. Fitzgerald, and K. Ryan, "Cylinders with square cross-section: wake instabilities with incidence angle variation," J. Fluid Mech. **630**, 43 (2009).

[5] A. Fage and F. C. Johansen, "On the flow of air behind an inclined flat plate of infinite span," Proc. R. Soc. London, Ser. A **116**, 170 (1927).
[6] K. M. Lam, "Phase-locked eduction of vortex shedding in flow past an inclined flat plate," Phys. Fluids **8**, 1159 (1996).
[7] A. E. Perry and T. R. Steiner, "Large-scale vortex structures in turbulent wakes behind bluff bodies. Part 1. Vortex formation," J. Fluid Mech. **174**, 233 (1987).
[8] K. M. Lam and M. Y. H. Leung, "Asymmetric vortex shedding flow past an inclined flat plate at high incidence," Eur. J. Mech. B/Fluids **24**, 33 (2005).
[9] M. Breuer and N. Jovicic, "Separated flow around a flat plate at high incidence: an LES investigation," J. Turbul. **2**, 1 (2001).
[10] M. Breuer, N. Jovicic, and K. Mazaev, "Comparison of DES, RANS and LES for the separated flow around a flat plate at high incidence," Int. J. Numer. Methods Fluids **41**, 357 (2003).
[11] J. Zhang, N.-S. Liu, and X.-Y. Lu, "Route to a chaotic state in fluid flow past an inclined flat plate," Phys. Rev. E **79**, 045306 (2009).
[12] M. Manhart, "A zonal grid algorithm for DNS of turbulent boundary layers," Comput. Fluids **33**, 435 (2004).
[13] N. Peller, A. L. Duc, F. Tremblay, and M. Manhart, "High-order stable interpolations for immersed boundary methods," Int. J. Numer. Methods Fluids **52**, 1175 (2006).
[14] F. M. Najjar and S. P. Vanka, "Effects of intrinsic three-dimensionality on the drag characteristics of a normal flat plate," Phys. Fluids **7**, 2516 (1995).
[15] V. D. Narasimhamurthy and H. I. Andersson, "Numerical simulation of the turbulent wake behind a normal flat plate," Int. J. Heat Fluid Flow **30**, 1037 (2009).
[16] D. Yang, B. Pettersen, H. I. Andersson, and V. D. Narasimhamurthy, "Three-dimensional transition to turbulence in the wake of an inclined flat plate," J. Phys.: Conf. Ser. **318**, 032044 (2011).
[17] Y. Hoarau, M. Braza, Y. Ventikos, D. Faghani, and G. Tzabiras, "Organized modes and the three-dimensional transition to turbulence in the incompressible flow around a NACA0012 wing," J. Fluid Mech. **496**, 63 (2003).
[18] V. Kitsios, "Recovery of fluid mechanical modes in unsteady separated flows," Ph.D. dissertation (The University of Melbourne and Université de Poitiers, 2010).
[19] C. H. K. Williamson, "The natural and forced formation of spot-like 'vortex dislocations' in the transition of a wake," J. Fluid Mech. **243**, 393 (1992).
[20] Z. Huang, V. D. Narasimhamurthy, and H. I. Andersson, "Oblique and cellular vortex shedding behind a circular cylinder in a bidirectional shear flow," Phys. Fluids **22**, 114105 (2010).
[21] V. D. Narasimhamurthy, H. I. Andersson, and B. Pettersen, "Cellular vortex shedding in the wake of a tapered plate," J. Fluid Mech. **617**, 355 (2008).
[22] V. D. Narasimhamurthy, H. I. Andersson, and B. Pettersen, "Cellular vortex shedding behind a tapered circular cylinder," Phys. Fluids **21**, 044106 (2009).
[23] J. Jeong and F. Hussain, "On the identification of a vortex," J. Fluid Mech. **285**, 69 (1995).
[24] H. Mansy, P.-M. Yang, and D. R. Williams, "Quantitative measurements of three-dimensional structures in the wake of a circular cylider," J. Fluid Mech. **270**, 277 (1994).
[25] S. Balachandar, R. Mittal, and F. M. Najjar, "Properties of the mean recirculation region in the wakes of two-dimensional bluff bodies," J. Fluid Mech. **351**, 167 (1997).
[26] W. C. Reynolds and A. K. M. F. Hussain, "The mechanics of an organized wave in turbulent shear flow. Part 3. Theoretical models and comparison with experiments," J. Fluid Mech. **54**, 263 (1972).
[27] B. Cantwell and D. Coles, "An experimental study of entrainment and transport in the turbulent near wake of a circular cylinder," J. Fluid Mech. **136**, 321 (1983).